

Graphene-inspired porous polymer network for ethane/ethylene separation and methane purification

Received: 29 August 2025

Accepted: 24 February 2026

Cite this article as: Festus, K., Guo, F., Ullah, S. *et al.* Graphene-inspired porous polymer network for ethane/ethylene separation and methane purification. *Nat Commun* (2026). <https://doi.org/10.1038/s41467-026-70471-7>

Kelechi Festus, Fuan Guo, Saif Ullah, Sayan Maiti, Ankit Mondal, Vladimir Bakhmutov, Urme Podder, Aishi Sikdar, Roknuzzaman Roknuzzaman, Hengyu Lin, Lei Fang, Shengqian Ma, Timo Thonhauser, Hao Wang, Qingsheng Wang & Hong-Cai Zhou

We are providing an unedited version of this manuscript to give early access to its findings. Before final publication, the manuscript will undergo further editing. Please note there may be errors present which affect the content, and all legal disclaimers apply.

If this paper is publishing under a Transparent Peer Review model then Peer Review reports will publish with the final article.

Graphene-Inspired Porous Polymer Network for Ethane/Ethylene Separation and Methane Purification

Kelechi Festus^{1,2}, Fuan Guo³, Saif Ullah⁴, Sayan Maiti⁵, Ankit Mondal¹, Vladimir Bakhmutov¹, Urme Podder¹, Aishi Sikdar¹, Roknuzzaman Roknuzzaman⁵, Hengyu Lin¹, Lei Fang¹, Shengqian Ma⁵, Timo Thonhauser⁴, Hao Wang³, Qingsheng Wang^{2*} & Hong-Cai Zhou^{1*}

¹Department of Chemistry, Texas A&M University, College Station, TX 77842, USA

²Artie McFerrin Department of Chemical Engineering, Texas A&M University, College Station, TX 77842, USA

³Hoffmann Institute of Advanced Materials, Shenzhen Polytechnic University, 7098 Liuxian Blvd., Shenzhen 518055, P. R. China

⁴Department of Physics and Center for Functional Materials, Wake Forest University, Winston-Salem, NC 27109, USA

⁵Department of Chemistry, University of North Texas, Denton, TX 76203, USA

Correspondence and requests for materials should be addressed to Q.W. and H.-C. Z.

*Email: qwang@tamu.edu; zhou@chem.tamu.edu

Abstract

C₂H₄ and CH₄ are essential for industrial applications. However, contamination with other natural gases is a challenge to their utilization. Although several sorbents have been investigated, their performance remains limited. This study introduces graphene-inspired, PPN-20, a porous polymer network (PPN) capable of separating C₂H₆/C₂H₄ and purifying CH₄ from a C₃H₈/C₂H₆/CH₄ mixture in a single step. The ultra-microporosity of PPN-20 enables preferential C-H... π interactions with C₂H₆ and C₃H₈. As a result, PPN-20 exhibits a C₂H₆ and C₃H₈ uptake of 3.93 mmol/g and 5.98 mmol/g, respectively, at 298 K and 1 bar, representing the highest reported for any PPN. It achieves ideal adsorption solution theory (IAST) selectivities of 2.2 for C₂H₆/C₂H₄, 368.2 for C₂H₆/CH₄, 40.14 for C₃H₈/C₂H₆, and 294,336 for C₃H₈/CH₄. This selectivity, to the best of our knowledge, is the highest reported for any PPN in the case of C₂H₆/C₂H₄ separation and for any sorbent in the cases of C₂H₆/CH₄, C₃H₈/C₂H₆, and C₃H₈/CH₄ separation. Robustness tests, including breakthrough experiments, IAST calculations, etc., demonstrate the reliability of PPN-20. Its exceptional performance is attributed to precisely engineered pore sizes that enhance the trapping of guest molecules. These results will pave the way for the design of PPNs for short-chain hydrocarbon purification.

Keywords: Gas Separation, PPNs, Energy and Sustainability, Ethane/Ethylene, Propane/Ethane/Methane

Introduction

The demand to curb the rising effects of greenhouse gas emissions has led to a very aggressive pursuit recently from government agencies and industries in response to global warming.¹⁻³ Methane, the second most abundant after carbon dioxide (CO₂) and a more potent greenhouse gas, has a global warming potential that is 21 times that of CO₂, but can also be used as a source of energy, making its capture and storage a dual-purpose achievement by mitigating global warming while providing an alternative energy source.⁴ Ethylene, on the other hand, is a vital feedstock for the production of polymer-based end products or materials used across household items, automobiles, and aviation facilities.⁵⁻⁷ Industrially, many downstream product development processes are energy-intensive, motivating the search for more efficient alternatives. Purifying ethylene and methane from other analog gases is essential, as ethylene is widely used in polymer manufacturing, while methane serves as an essential energy resource to drive industrialization and curb global warming.⁸⁻¹⁰ Currently, ethylene and methane purification are predominantly achieved through cryogenic distillation processes that are energy-intensive, highlighting the need

for an alternative route.¹¹⁻¹⁴ Rising energy prices render this strategy unfeasible for long-term commercial application in industry, thereby driving the exploration of different kinds of sorbent materials for ethylene and methane purification.

Furthermore, the quest for alternative energy sources and solutions to global warming has made methane crucial. However, the primary challenge in utilizing methane lies in its harvesting, capture, and purification. Natural gases contain varying percentages of hydrocarbons, which limits direct utilization and hence the need for further purification steps.¹⁵ Ethane and propane are among the major contaminants in natural gas and must be effectively removed to boost the purity of methane, since it cannot be used without their removal, because they lead to explosion risk due to reduced ignition delay.

Ethane/ethylene separation through cryogenic distillation remains critical in meeting the industrial demand for ethylene in the production of several high-end polymer-based materials. This process amounts to the consumption of about 800 PJ annually, which corresponds to about 0.3% of global energy utilization.^{13,16} Ethylene, a major industrial feedstock, is notoriously produced through the energy-intensive thermal cracking of hydrocarbons.^{17,18} To reduce energy footprint, the development of sorbents for the purification of ethylene from ethane has drawn the attention of researchers. However, one of the major drawbacks in this direction is achieving the selective capture of ethane over ethylene, which will enable a single-step purification.^{19,20} Several adsorbents have been reported in this regard, but many suffer from weak selectivity for ethane/ethylene^{9,21,22} or poor ethane uptake capability^{23,24} that limits their commercialization and industrial application. The rational design of sorbents for this application requires the consideration of the quadrupole moment of ethylene (1.50×10^{-26} esu cm²) relative to ethane (0.65×10^{-26} esu cm²), polarizability difference (ethylene: 42.52×10^{-25} cm³; ethane: 44.7×10^{-25} cm³), and the presence of π electrons.²⁵ The design of an ethane-selective adsorbent requires the pores to be nonpolar to boost the trapping of ethane guests in the pores.

Sorbents such as Metal-Organic Frameworks (MOFs),^{19,26} Hydrogen Organic Framework (HOF),²⁷ and Porous Organic Cage (POC)²⁸ have been explored in the process to seek a solution to this problem. However, PPNs remain relatively underexplored. PPNs are a group of sorbent materials that have shown significant application in the capture and separation of gas molecules.²⁹⁻³² PPNs have undergone several modifications to achieve target goals such as carbon capture³³ and heavy metal recovery³⁴ but their applications in methane purification from alkanes, and ethane/ethylene separation have not been explored as extensively as MOFs^{35,36}. Fundamentally, PPNs are a class of porous materials that are made from the polymerization of organic monomers, resulting in voids suitable for the capture of gaseous molecules. The tunability, stability, and robustness of these pores to fit the kinetic diameters of target gases and their re-engineering through post-synthetic modification make PPNs very exceptional. MOFs differ from PPNs as a type of sorbent material made from metal nodes and organic linkers to grow porous crystalline moieties, whose downsides are the high cost of starting materials, high reaction temperature, and low chemical and thermal stability, which makes PPNs stand out.³⁷ Additionally, MOFs and COFs differ from PPNs because they are crystalline materials formed due to the reversibility of their bonds, while PPNs possess irreversible bonds and are therefore amorphous.

Herein, we design a robust PPN, PPN-20, featuring a graphene-inspired structure with an effective pore size distribution, excellent thermal and chemical stability, and facile reaction conditions requirements for C₂H₆/C₂H₄ separation and CH₄ purification from a mixture of C₃H₈/C₂H₆/CH₄. This is the first time, to the best of our knowledge, that PPN has been developed for this kind of ultra-sensitive two-fold application. PPN-20 exhibits the highest performance among the PPNs reported for these applications. As a result, it will increase the availability of ethylene and methane as key industrial feedstocks and significantly reduce the energy footprint of industries. Importantly, this study will open the door for research into PPNs for efficient natural gas separation.

Results and Discussion

Pore Structure and Morphology of PPN-20

To understand the morphology of the pores, present in PPN-20 (Fig 1a), small-angle X-ray scattering (SAXS) analysis was conducted. Based on single-component gas adsorption, the pores of this sorbent are ultra-microporous and microporous and, consequently, aid in the high gas uptake and selectivity capability of PPN-20. This is corroborated by the radius of gyration (R_g) value ($14 \text{ \AA} = 1.4 \text{ nm}$) derived from the Guinier approximation of the SAXS result (Fig. 1b), which closely matches the pore size distribution derived from the gas uptake measurement.

Interestingly, the Porod approximation with a power law exponent of 2.13 indicates that the pores are not smooth but have fractal surfaces, possibly caused by the irregularity of the pore pattern encountered during the polymerization process (Fig. 1c). This conclusion is supported by the power law coefficient being below 4 in the high Q region because of the amorphous nature of the PPN-20, and the inherent interpenetration that makes it difficult to know the exact shape of the pores.

Framework Structure and Characterization

PPN-20 has porosity that is periodically surrounded by the six-membered benzene rings and derived from the triple condensation reaction of the acetyl groups of 1,3,5-triacetyl benzene (Supplementary Fig. 1-2). After the reaction, the resulting material adopts a graphene-inspired hypercross-linked structure, which has quasi-periodic pores that facilitate gas adsorption. The van der Waals density functional (vdW-DF) level theoretical simulation results show a pore of 3.782 \AA (0.3782 nm) (which is $\sim 5.7 \text{ \AA}$ (0.57 nm) without the hydrogen atoms, as shown in Fig. 1a) and a C–C bond length of 1.509 \AA in a completely formed aromatic benzene ring and 1.409 \AA in an open ring (Fig. 2a). The calculated C–H bond length is 1.08 \AA (Fig. 2a). Additionally, the side view indicates that the hydrogen atoms are pointing 0.8 \AA away from the framework—so, the sheet has a tendency to buckle (Fig. 2b). Specifically, the monomer was polymerized into a hyper-crosslinked PPN made up mainly of carbon and hydrogen as confirmed by Fourier Transform Infrared Spectroscopy (FTIR) and Solid-state Nuclear Magnetic Resonance (ss-NMR) (Supplementary Fig. 3a-4b).

PPN-20 demonstrated high chemical stability when exposed to water, acid, base, and various organic solvents for 24 hours, which highlights its robustness for gas separation applications even in a harsh chemical environment (Supplementary Figs. 3b-3c). The C-H and O-H vibrational stretching, which appeared centered at 2981 cm^{-1} and 3391 cm^{-1} , respectively, are from the ethanol used to wash the sample. The comparison of the $^{13}\text{C} \{^1\text{H}\}$ CP MAS NMR spectra of 1,3,5-triacetylbenzene (top) and PPN-20 (bottom) recorded at a spinning rate of 12 kHz was analyzed (Supplementary Figure 4b). As seen, 1,3,5-triacetylbenzene shows the sharp resonances with $\delta(\text{iso})$ of 200.0 and 197.5 ppm (C=O), 148.7, 134.7, 133.1, and 130.6 ppm (aromatic carbons) and 29.2 and 27.9 ppm (CH_3). Furthermore, for PPN-20, which has a polymer nature, all the resonances are reasonably broadened, experiencing slight displacements: $\delta(\text{iso})$ of 200.6 ppm (C=O), 142.5, 139.5, 131.4, and 126.4 ppm (aromatic carbons) and 26.7 ppm (CH_3).

Transmission Electron Microscopy (TEM) and Scanning Electron Microscopy (SEM) reveal both the hypercross-linked morphology of PPN-20 and the stacking of the various layers, which obscure the direct visualization of the individual pores present in the framework (Supplementary Fig. 5-6). The hypercross-linking substantially enhances the thermal and chemical stability of the framework compared to the starting monomer, ensuring that it can withstand both harsh thermal and chemical conditions. To elucidate the chemical stability of PPN-20 for potential industrial application, it was soaked in acid, base water, and organic solvents, but showed no sign of solubility as aforementioned. The thermal stability of PPN-20 is up to 360°C , as seen from thermogravimetric analysis (TGA) in Supplementary Fig. 7. Due to the stacking and interpenetration of several layers of the framework, the Powder X-ray Diffraction (PXRD) pattern shows no diffraction peaks, confirming that PPN-20 is an amorphous solid (Supplementary Fig. 8).

Gas Adsorption, Selectivity, Separation, and Enthalpy of Adsorption

The pore-based properties of PPN-20 were studied extensively through a single-component gas uptake measurement. The nitrogen (N_2) uptake and pore distribution measurement were conducted at 77 K and 1 bar to determine the surface area and pore-size distribution (Fig. 3a). It was observed to have a permanent porosity with

a pore volume of 0.94 cm³/g, and a surface area of 1679 m²/g (Supplementary Table 1). The N₂ Isotherm of PPN-20 has a type I adsorption isotherm due to the presence of predominantly ultra-small pores. The pore size distribution shows a sharp peak at 0.5 nm and other pores between 0.6 nm to 0.9 nm (Fig. 3b). The sharp peak at 0.5 nm indicates that PPN-20 is not only microporous but also exhibits ultra-microporosity. The sizes of these pores contributed immensely to the enhanced gas uptake, selectivity, and the observed isosteric heat of adsorption (Q_{st}) (Fig. 3c and 3d).

Due to the absence of unsaturated bonds in C₂H₆, it is more polarizable and has a larger kinetic diameter than C₂H₄, which gives it a preference for specific pores and inherently increases its selectivity in PPN-20. PPN-20, to the best of our knowledge, has the highest selectivity of C₂H₆/C₂H₄ ever reported for any PPN to date due to the presence of ultra-micropores. This factor also contributed to the higher surface area that it has, even higher than any PPN made using the facile aldol triple condensation (ATC) reaction route reported by Fang et al.³⁸ The presence of both ultra-microporous and microporous pores in PPN-20 motivated the further investigation of its ability to adsorb other gases such as methane, propane, ethane, and ethylene. To this effect, the uptake of these gases was studied at 273 K and 298 K at 1 bar. Impressively, PPN-20 showed 3.93 mmol/g, 3.56 mmol/g, 5.98 mmol/g, and 0.80 mmol/g uptake for C₂H₆, C₂H₄, C₃H₈, and CH₄, respectively, at 298 K and 1 bar (Supplementary Figs. 9, 10, 14, 18, 22).

The IAST selectivity calculation was performed for various mixtures of gases. The selectivity of C₃H₈/CH₄, C₂H₆/CH₄, C₃H₈/C₂H₆, and C₂H₆/C₂H₄ in a 50:50 (1:1) v/v mixture is 294, 336.12, 368.16, 40.14, and 2.2, while the separation potential from the experimental single-component gas adsorption is 5.18, 3.13, 2.05, and 0.37, respectively, at 298 K and 1 bar (Supplementary Fig. 10-25 and Supplementary Table 2). The C₂H₆/C₂H₄ IAST selectivity of PPN-20 is significantly higher than the state-of-the-art PAN-AN³⁹ and surpasses all previously reported sorbents for C₃H₈/CH₄, C₂H₆/CH₄, and C₃H₈/C₂H₆ (Supplementary Table 3-6). Comparison of these performances with other sorbents indicates that PPN-20 is superior in performance and is a good candidate for industrial application or commercialization (Supplementary Figs. 13, 17, 21, and 25). The Q_{st} was also computed to validate the selectivity. At zero coverage, C₃H₈, C₂H₆, C₂H₄, and CH₄ had a Q_{st} of 81.7 kJ/mol, 43.04 kJ/mol, 35.9 kJ/mol, and 16.25 kJ/mol respectively, which decreased to 27.9 kJ/mol, 22.6 kJ/mol, 17.3 kJ/mol, and 13.3 kJ/mol at 1 bar (Supplementary Figs. 26-30).

To validate the practical application of the IAST selectivity result of PPN-20, breakthrough measurements were conducted at 298 K and 1 bar for C₂H₆/C₂H₄ and C₃H₈/C₂H₆/CH₄ mixtures since these conditions replicate the industrial scenario. This experiment was conducted for C₂H₆/C₂H₄ and C₃H₈/C₂H₆/CH₄ in a mixture ratio of 50:50 (v/v) and 30:30:40 (v/v/v), respectively (Fig. 4a and 4b). PPN-20 was packed in a column, and as observed from the breakthrough curve, the C₂H₄ breaks before C₂H₆ after a significant time-lapse (Fig. 4a), which shows that PPN-20 can purify a gas mixture of C₂H₆/C₂H₄ and produce a pure outflow of C₂H₄ due to the molecular sieving effect of the sorbent. The mass spectrometer connected to the breakthrough instrument showed that C₂H₄ has more than 99% purity. It also demonstrated efficiency in the separation of a ternary mixture of C₃H₈/C₂H₆/CH₄, where the methane gas breaks first, followed sequentially by C₂H₆ and C₃H₈, attesting to the molecular sieving effect driving the performance. The breakthrough pattern observed in the C₃H₈/C₂H₆/CH₄ mixture is consistent with the kinetic diameter of each of the gases, which enabled the molecule with the smallest size to break first before the others. In the breakthrough experiment of C₃H₈/C₂H₆/CH₄ (30/30/40, v/v/v), the productivity for CH₄ (purity > 99.5%) is 17.6 L kg⁻¹, and the dynamic adsorption capacities for C₂H₆ and C₃H₈ are 5.4 and 50.2 L kg⁻¹, respectively while in the breakthrough experiment of C₂H₄/C₂H₆, (50:50, v/v) the productivity for C₂H₄ (99.5%) is 0.63 L kg⁻¹, and the dynamic adsorption capacity for C₂H₆ is 21.4 L kg⁻¹. The robustness of PPN-20 was further investigated to ascertain its capacity through five (5) breakthrough cycles of the binary (C₂H₆/C₂H₄) and ternary (C₃H₈/C₂H₆/CH₄) gas mixtures. The breakthrough curve after five (5) cycles stayed consistent without any noticeable reduction or depreciation in the efficiency of PPN-20 in both C₂H₆/C₂H₄ and C₃H₈/C₂H₆/CH₄. This observation elucidates the robustness of PPN-20 and its potential for industrial application (Fig. 4c and 4d).

Binding Mechanism, Gas Separation, and Molecular Sieving Effect

The binding mechanism was investigated using the help of the electron localization function (ELF), which reveals a strong covalent C–C bond within the framework (Supplementary Fig. 31). To ascertain this, various theoretical bilayer stacking configurations were investigated to elucidate how the pores are influenced by them (Supplementary Figs. 32-34). As mentioned above, the pores in the framework facilitate the adsorption of small guest molecules. Since the exact structure is not known, it was studied by exposing a simplified model, i.e., a local geometry of a single sheet of the framework, to the C1–C3 hydrocarbons CH₄, C₂H₄, C₂H₆, and C₃H₈ and calculating their binding energy. Two distinct binding sites were found for the guest molecules: one is on top of the pore region and the other at framework atoms (see Supplementary Figs. 33 and 34). Our calculations suggest that the pore sites are more favorable, and we refer to them as the primary binding sites. The binding energies at this location at full loading are 0.382 eV, 0.336 eV, 0.290 eV, and 0.183 eV for C₃H₈, C₂H₆, C₂H₄, and CH₄ (Supplementary Table 7). The interaction with guest molecules is energetically still preferable at the secondary binding site on top of framework atoms (Supplementary Fig. 34); at that location, the binding energies were found to be 0.289 eV, 0.221 eV, 0.177 eV, and 0.131 eV (Supplementary Table 7). The reduction in binding energy at the secondary binding site is consistent with the increased separation of the guest molecules from the framework (Supplementary Fig. 12, 16, 20, and 24). Consistently, these calculations successfully reproduced the binding trend observed in the experimental isotherm measurements.

The binding mechanism was further analyzed for the various gas molecules through induced charge densities, i.e., the charge rearrangement upon interaction with the framework, shown in Supplementary Figs. 35-36. These induced charge densities show a stronger interaction with the guest molecules at the primary sites compared to secondary sites and follow the exact trend in binding strength. For completeness and accuracy, the intercalation behavior of the largest guest molecule studied—propane—within the graphene-inspired PPN-20 was also analyzed. Both the primary and secondary adsorption sites exhibit favorable binding energies for propane. Notably, the results obtained are consistent not only qualitatively but also quantitatively, with bulk binding energies only ~10% lower than those of the monolayer. Propane adsorption induces a pronounced expansion of the interlayer spacing relative to the original interlayer distance of 3.752 Å. This is because occupation of the primary binding site increases the separation to 6.471 Å, reflecting a substantial structural response to the inclusion of the guest molecule. An even greater expansion is observed when propane resides at the secondary binding site, where the interlayer spacing reaches 7.115 Å. This larger displacement suggests that the secondary site exerts a stronger perturbation on the host framework, likely arising from distinct steric constraints and adsorption geometries. Collectively, these findings demonstrate the high sensitivity of the layered structure to molecular intercalation and highlight the structural flexibility of PPN-20 that makes it suitable for the adsorption and separation of these gases whose kinetic diameters are within a close range (Supplementary Table 8).

Discussion

In summary, we reported a PPN-20 that possesses a combined inherent capability to purify both a binary C₂H₆/C₂H₄ and a ternary CH₄/C₂H₄/C₃H₈ gas mixture. This was achieved through rational pore engineering of the sorbent to adopt a molecular sieving effect to extrude gas molecules based on their physical properties. PPN-20 is a hyper-cross-linked polymer that has significantly high thermal and chemical stability, making it suitable for use in a harsh environment. It exhibits a higher affinity for C₂H₆ and C₃H₈ due to their favorable fit within its pore structures. The binding energy calculation is also consistent with the observed selectivity and Q_{st} results. Overall, PPN-20 has the highest selectivity for C₂H₆ among all PPNs reported to date and C₃H₈ (useful for methane purification) among all reported sorbents. Consequently, these results will pave the way for the engineering of PPNs for natural gas separation, a scarcely explored path. Efforts to explore its industrial applications are underway. Although interpenetration during the polymerization and different stacking patterns of the various layers make it difficult to view the individual pores, PPN-20 remains a robust graphene-inspired material for natural gas separation and purification.

Methods

Synthesis of PPN-20: Methane sulfonic acid was supplied by ThermoFisher Scientific, while 1,3,5-triacetylbenzene was purchased from TCI. All reagents were analytical grade and used without further purification. 1,3,5-triacetylbenzene (2.0 g, 0.979 mmol) and methane sulfonic acid (13 ml, 200.3 mmol) were added to a 50 ml hydrothermal autoclave. Without preheating to homogenize the mixture, as reported by Fang et al³⁸, the vial was then transferred to an oven and heated at 120°C for 24 hours. After cooling to room temperature, water was added to quench the reaction. The monolith was thoroughly washed with water and ethanol. Finally, the dark solid product was crushed and heated in a sand bath to evaporate the solvents. The dried mass of the solid is 1.78 g (~89% yield).

Sample Characterization: The electron imaging of PPN-20 was done to study the morphology and stacking of the various layers after the reaction. A combination of Titan Themis³ 300 S/TEM and FE-SEM: "(JSM7500, RRID: SCR_022202) was utilized for TEM and SEM studies, respectively. FTIR of the PPN was performed using a Shimadzu IRAffinity-1 spectrometer. TGA was conducted at a ramp rate of 5°C/min under dynamic nitrogen flow over a temperature range of 25-900°C by a Mettler-Toledo TGA/DSC 1. PXRD was measured at room temperature with a Powder-ECO Bragg-Brentano Theta/Theta diffractometer equipped with a Lynxeye detector XT.

Small-Angle X-ray Scattering: The nature of the pore surface was studied using a SAXS (Xenocs Xeuss 3.0 system, France). Before the analysis, the powder sample was packed into a 1 mm thick washer with two faces covered with Capton windows. The scattering pattern was obtained at room temperature. It has a Dectris Eiger 2R 1M-pixel 2D detector and is equipped with a GeniX 3D X-ray beam delivery system. The SAXS beam was from a monochromatic Cu K α ($\lambda = 1.54$) high-intensity X-ray beam. A sample-to-detector distance of 900 mm was maintained. The exposure time was 20 minutes and the 2D scattering patterns were acquired with a line-eraser mode and then reduced into 1D plots after calibration with LaB₆ and silver behenate standards. Guinier and Porod laws equations were used in fitting the SAXS data to determine the radius of gyration, scattering vector, and scattering intensity.⁴⁰⁻⁴² The equations are given as follows:

Guinier law:

$$I(q) = I(0) \exp\left(-\frac{q^2 R_g^2}{3}\right) \quad (1)$$

Porod law:

$$I(q) \sim q^{-4} \quad (2)$$

Where $I(q)$ (unit: cm^{-1}) is the scattering intensity, $I(0)$ (unit: cm^{-1}) is the intensity when $q = 0$ and is usually referred to as the forwarding intensity, q (unit: \AA^{-1}) is the scattering vector, and R_g (unit: \AA) is the radius of gyration. The equation for the scattering vector is:

$$q = \frac{4\pi}{\lambda} \sin(\theta) \quad (3)$$

Where λ (unit: \AA) is the incident radiation wavelength and θ (unit: degree) is the scattering angle. **Note:** The SASview 5.0.4 software was used to process the data.

Solid-State NMR: The ¹³C {¹H} MAS ss-NMR experiments were carried out with a Bruker Avance-NEO ss-NMR spectrometer (400 MHz for ¹H nuclei) equipped with a standard two-channel 4 mm MAS probe head. The external reference was C₆D₆ (128.6 ppm). The ¹³C {¹H} CP MAS NMR spectra were obtained at a spinning rate from 8 to 12 kHz with a standard cross-polarization pulse sequence at ¹H pulse of 2.5 μs 90°, CP contact time of 4.0 ms (power of 77.2 W), and relaxation delays of 8 s. The standard tppm15 pulse sequence has been used for high-power ¹H decoupling.

Gas Uptake Measurement: The pore size and surface area were determined using Micromeritics ASAP 2020 surface area and porosity analyzer. Ultra-high purity (UHP) nitrogen was used to determine the surface area and pore size distribution at 77 K and 1 bar. The uptake of propane, ethane, ethylene, and methane at 1 bar was also measured at 298 K and 273 K, respectively. Before this, the sample was degassed at 120°C for 600 minutes. The pore size distribution was determined using MicroActive software (Micromeritics), assuming slit-pore geometry for the analysis. The sample tubes were properly cleaned before use to avoid contamination and interference with the measurement.

IAST Selectivity: The selectivity of C₃H₈/CH₄, C₂H₆/CH₄, C₃H₈/C₂H₆, and C₂H₆/C₂H₄ (supplementary table 2) was calculated from the single-component adsorption data measured at 298 K. The adsorption data were fitted with the Extended Langmuir equation below.

$$y = \frac{a \cdot b \cdot p^{1-c}}{1 + b \cdot p^{1-c}} \quad (4)$$

Where y (mmol/g) is the amount of gas adsorbed on the surface per gram of the sorbent, a (mmol/g) is the maximum adsorption capacity of the sorbent. b (1/kPa) is the Langmuir constant. p refers to the normalized pressure of the adsorbate gas. c represents a deviation from an ideal homogeneous surface and is dimensionless. The plots of the fitted parameters were used to calculate the selectivity of the gas mixtures (Supplementary Fig. 11, 15, 19, 23). The IAST selectivity (Supplementary Table 2) was calculated from the Myers and Prausnitz⁴³ equation below and the Extended Langmuir fitting parameters.

$$S_{\text{ads}} = \frac{q_1/q_2}{p_1/p_2} \quad (5)$$

q_1 and q_2 are the mole fractions of the adsorbed bulk phase at any specific pressures (p_1 and p_2).

Binary Gas Separation Potential

Separation potential can be calculated for PPN-20 since the single-component adsorption has been experimentally collected, fitted, and used to determine the IAST selectivity at 298 K and 1 bar necessary for the computation.^{44,45}

Using the experimental uptake:

$$\Delta q_{\text{exp}} = q_1 - q_2 \quad (6)$$

Using the equimolar mixture:

$$\Delta q = q_1 \left(1 - \frac{y_1}{y_2 S} \right) \quad (7)$$

or

$$\Delta q = q_1 \left(1 - \frac{1}{S} \right) \quad (8)$$

S = IAST Selectivity. q_1 = Amount of preferred gas molecules adsorbed at a specific temperature and pressure. q_2 = Amount of less preferred gas molecules adsorbed at a specific temperature and pressure. y_1, y_2 = Mole fraction of the gas molecules adsorbed.

Isosteric Enthalpy of Adsorption: The interaction between the surface of the sorbent and adsorbate gases is represented by the Q_{st} . The single-component adsorption was measured at 273 K and 298 K and fitted with the Langmuir-Freundlich equation below.

$$y = \frac{a \cdot b \cdot p^c}{1 + b \cdot p^c} \quad (9)$$

Where y (mmol/g) is the adsorbed quantity. P (kPa) is the pressure. a (mmol/g) is the adsorption capacity and b ($1/\text{kPa}^c$) are the strength of the affinity between the adsorbate and the adsorbent. c represents a deviation from an ideal homogeneous surface and is dimensionless. Based on the fitting parameters, the Q_{st} was determined from the Clausius-Clapeyron equation given below:

$$\frac{\partial(\ln P)}{\partial(1/T)} = -\frac{Q_{\text{st}}}{R} \quad (10)$$

Where p is gas pressure, R is the universal gas constant, T is the temperature of adsorption, and Q_{st} is the enthalpy of adsorption (Supplementary Fig. 30).

Structure Simulation and Binding Energy: All *ab initio* calculations were performed with the help of the VASP code.^{46,47} The standard projector augmented wave (PAW) pseudopotentials were used with a plane-wave basis set formalism. The kinetic energy cutoff was set to 600 eV, and the Brillouin zone was sampled with a Gamma-centered $5 \times 5 \times 1$ k-point grid. To capture dispersion forces accurately in layered systems, we used a fully non-local vdW-DF1 functional in all calculations.⁴⁸ The geometries were considered converged when the forces on each atom were less than 0.005 eV/Å. The energy convergence criterion for the SCF cycle was 10^{-6} eV. The geometries were first relaxed with a conjugate gradient (CG) algorithm and later re-relaxed with a more robust Quasi-Newton (QN) optimizer.

Breakthrough Experiment: Breakthrough tests were carried out in an auto mixed-gas breakthrough apparatus (3P MIXSORB). The weight of all test samples packed into the column (I.D. 6 mm, volume 2 mL) was approximately 0.5 g. The packed adsorbent was activated by heating to 120°C for 5 h under helium flow (10 mL/min). The mixed gases ($\text{C}_2\text{H}_6/\text{C}_2\text{H}_4$ (50/50, v/v); $\text{C}_3\text{H}_8/\text{C}_2\text{H}_6/\text{CH}_4$ (30/30/40, v/v/v)) at a flow rate of 2 mL/min and a helium gas at a flow rate of 6 mL/min were switched to pass through the adsorption bed. The outlet gas was analyzed by using a mass spectrometer (MKS).

Data Availability

All experimental and computational data supporting the findings of this study are included in the published article, supplementary information, and source data. Upon request, they can also be obtained from the corresponding authors. Source data are provided as a Source Data file.

References

- Peter, S. C. Reduction of CO₂ to Chemicals and Fuels: A Solution to Global Warming and Energy Crisis. *ACS Energy Letters* **3**, 1557-1561, doi:10.1021/acseenergylett.8b00878 (2018).
- Simmer, R. A., Jansen, E. J., Patterson, K. J. & Schnoor, J. L. Climate Change and the Sea: A Major Disruption in Steady State and the Master Variables. *ACS Environmental Au* **3**, 195-208, doi:10.1021/acsenvironau.2c00061 (2023).
- Xu, W. *et al.* Globally elevated greenhouse gas emissions from polluted urban rivers. *Nature Sustainability*, doi:10.1038/s41893-024-01358-y (2024).
- Chang, M. *et al.* Enhancing CH₄ Capture from Coalbed Methane through Tuning van der Waals Affinity within Isorecticular Al-Based Metal–Organic Frameworks. *ACS Applied Materials & Interfaces* **14**, 25374-25384, doi:10.1021/acscami.2c03619 (2022).
- Goller, A., Obenauf, J., Kretschmer, W. P. & Kempe, R. The Highly Controlled and Efficient Polymerization of Ethylene. *Angewandte Chemie International Edition* **62**, e202216464, doi:https://doi.org/10.1002/anie.202216464 (2023).
- Zhang, Y., Kang, X. & Jian, Z. Selective branch formation in ethylene polymerization to access precise ethylene-propylene copolymers. *Nature Communications* **13**, 725, doi:10.1038/s41467-022-28282-z (2022).

- 7 Chen, Z., Leatherman, M. D., Daugulis, O. & Brookhart, M. Nickel-Catalyzed Copolymerization of Ethylene and Vinyltrialkoxysilanes: Catalytic Production of Cross-Linkable Polyethylene and Elucidation of the Chain-Growth Mechanism. *Journal of the American Chemical Society* **139**, 16013-16022, doi:10.1021/jacs.7b10281 (2017).
- 8 Wang, S.-M. *et al.* Ethane/Ethylene Separations in Flexible Diamondoid Coordination Networks via an Ethane-Induced Gate-Opening Mechanism. *Journal of the American Chemical Society* **146**, 4153-4161, doi:10.1021/jacs.3c13117 (2024).
- 9 Zhang, X. *et al.* Selective Ethane/Ethylene Separation in a Robust Microporous Hydrogen-Bonded Organic Framework. *Journal of the American Chemical Society* **142**, 633-640, doi:10.1021/jacs.9b12428 (2020).
- 10 Niu, Z. *et al.* A Metal–Organic Framework Based Methane Nano-trap for the Capture of Coal-Mine Methane. *Angewandte Chemie International Edition* **58**, 10138-10141, doi:<https://doi.org/10.1002/anie.201904507> (2019).
- 11 Hamed, H., Karimi, I. A. & Gundersen, T. Optimal cryogenic processes for nitrogen rejection from natural gas. *Computers & Chemical Engineering* **112**, 101-111, doi:<https://doi.org/10.1016/j.compchemeng.2018.02.006> (2018).
- 12 Rufford, T. E. *et al.* The removal of CO₂ and N₂ from natural gas: A review of conventional and emerging process technologies. *Journal of Petroleum Science and Engineering* **94-95**, 123-154, doi:<https://doi.org/10.1016/j.petrol.2012.06.016> (2012).
- 13 Sholl, D. S. & Lively, R. P. Seven chemical separations to change the world. *Nature* **532**, 435-437 (2016).
- 14 Ren, T., Patel, M. & Blok, K. Olefins from conventional and heavy feedstocks: Energy use in steam cracking and alternative processes. *Energy* **31**, 425-451, doi:<https://doi.org/10.1016/j.energy.2005.04.001> (2006).
- 15 Ghorbanian, K. & AminiMagham, M. Swirl intensity as a control mechanism for methane purification in supersonic gas separators. *Journal of Natural Gas Science and Engineering* **83**, 103572, doi:<https://doi.org/10.1016/j.jngse.2020.103572> (2020).
- 16 Mohamed, M. H. *et al.* Designing open metal sites in metal–organic frameworks for paraffin/olefin separations. *Journal of the American Chemical Society* **141**, 13003-13007 (2019).
- 17 Amghizar, I., Vandewalle, L. A., Van Geem, K. M. & Marin, G. B. New Trends in Olefin Production. *Engineering* **3**, 171-178, doi:<https://doi.org/10.1016/J.ENG.2017.02.006> (2017).
- 18 Corma, A. *et al.* Crude oil to chemicals: light olefins from crude oil. *Catalysis Science & Technology* **7**, 12-46, doi:10.1039/C6CY01886F (2017).
- 19 Liao, P.-Q., Zhang, W.-X., Zhang, J.-P. & Chen, X.-M. Efficient purification of ethene by an ethane-trapping metal-organic framework. *Nature Communications* **6**, 8697, doi:10.1038/ncomms9697 (2015).
- 20 Pillai, R. S., Pinto, M. L., Pires, J., Jorge, M. & Gomes, J. R. B. Understanding Gas Adsorption Selectivity in IRMOF-8 Using Molecular Simulation. *ACS Applied Materials & Interfaces* **7**, 624-637, doi:10.1021/am506793b (2015).
- 21 Lv, D. *et al.* Selective Adsorption of Ethane over Ethylene in PCN-245: Impacts of Interpenetrated Adsorbent. *ACS Applied Materials & Interfaces* **10**, 8366-8373, doi:10.1021/acsami.7b19414 (2018).
- 22 Böhme, U. *et al.* Ethene/Ethane and Propene/Propane Separation via the Olefin and Paraffin Selective Metal–Organic Framework Adsorbents CPO-27 and ZIF-8. *Langmuir* **29**, 8592-8600, doi:10.1021/la401471g (2013).
- 23 Liu, W. *et al.* Highly Robust Microporous Metal-Organic Frameworks for Efficient Ethylene Purification under Dry and Humid Conditions. *Angewandte Chemie International Edition* **62**, e202217662, doi:<https://doi.org/10.1002/anie.202217662> (2023).
- 24 Gücüyener, C., van den Bergh, J., Gascon, J. & Kapteijn, F. Ethane/Ethene Separation Turned on Its Head: Selective Ethane Adsorption on the Metal–Organic Framework ZIF-7 through a Gate-Opening Mechanism. *Journal of the American Chemical Society* **132**, 17704-17706, doi:10.1021/ja1089765 (2010).
- 25 Li, J.-R., Kuppler, R. J. & Zhou, H.-C. Selective gas adsorption and separation in metal–organic frameworks. *Chemical Society Reviews* **38**, 1477-1504, doi:10.1039/B802426J (2009).
- 26 Lin, R.-B. *et al.* Boosting Ethane/Ethylene Separation within Isoreticular Ultramicroporous Metal–Organic Frameworks. *Journal of the American Chemical Society* **140**, 12940-12946, doi:10.1021/jacs.8b07563 (2018).
- 27 Yang, Y. *et al.* Ethylene/ethane separation in a stable hydrogen-bonded organic framework through a gating mechanism. *Nature Chemistry* **13**, 933-939, doi:10.1038/s41557-021-00740-z (2021).
- 28 Su, K., Wang, W., Du, S., Ji, C. & Yuan, D. Efficient ethylene purification by a robust ethane-trapping porous organic cage. *Nature Communications* **12**, 3703, doi:10.1038/s41467-021-24042-7 (2021).

- 29 Patel, H. A. *et al.* Unprecedented high-temperature CO₂ selectivity in N₂-phobic nanoporous covalent organic polymers. *Nature Communications* **4**, 1357, doi:10.1038/ncomms2359 (2013).
- 30 Kuecken, S. *et al.* Fast tuning of covalent triazine frameworks for photocatalytic hydrogen evolution. *Chemical Communications* **53**, 5854-5857, doi:10.1039/C7CC01827D (2017).
- 31 Zou, L. *et al.* Porous Organic Polymers for Post-Combustion Carbon Capture. *Advanced Materials* **29**, 1700229, doi:<https://doi.org/10.1002/adma.201700229> (2017).
- 32 Day, G. S. *et al.* Improving Alkylamine Incorporation in Porous Polymer Networks through Dopant Incorporation. *Advanced Sustainable Systems* **3**, 1900051, doi:<https://doi.org/10.1002/adsu.201900051> (2019).
- 33 Lu, W. *et al.* Sulfonate-Grafted Porous Polymer Networks for Preferential CO₂ Adsorption at Low Pressure. *Journal of the American Chemical Society* **133**, 18126-18129, doi:10.1021/ja2087773 (2011).
- 34 Tang, Y. *et al.* Porous organic polymers for drug delivery: Hierarchical pore structures, variable morphologies, and biological properties. *Biomaterials Science* **10**, 5369-5390 (2022).
- 35 Chang, M., Ren, J., Yang, Q. & Liu, D. A robust calcium-based microporous metal-organic framework for efficient CH₄/N₂ separation. *Chemical Engineering Journal* **408**, 127294, doi:<https://doi.org/10.1016/j.cej.2020.127294> (2021).
- 36 Chang, M. *et al.* Separation of CH₄/N₂ by an ultra-stable metal-organic framework with the highest breakthrough selectivity. *AIChE Journal* **68**, e17794, doi:<https://doi.org/10.1002/aic.17794> (2022).
- 37 Vikrant, K., Kumar, V., Kim, K.-H. & Kukkar, D. Metal-organic frameworks (MOFs): potential and challenges for capture and abatement of ammonia. *Journal of Materials Chemistry A* **5**, 22877-22896, doi:10.1039/C7TA07847A (2017).
- 38 Guo, Z.-H. *et al.* Cost-effective synthesis and solution processing of porous polymer networks through methanesulfonic acid-mediated aldol triple condensation. *Materials Chemistry Frontiers* **2**, 396-401, doi:10.1039/C7QM00485K (2018).
- 39 Wang, C., Yan, J., Ma, Z. & Wang, Z. Highly efficient separation of ethylene/ethane in microenvironment-modulated microporous polymers. *Separation and Purification Technology* **287**, 120580, doi:<https://doi.org/10.1016/j.seppur.2022.120580> (2022).
- 40 Pak, S., Ahn, J. & Kim, H. Synthesis of Saccharide-based Hydrochar with Macroporous Structure for Effective Organic Pollutant Removal. *Fibers and Polymers* **23**, 1789-1796, doi:10.1007/s12221-022-4007-5 (2022).
- 41 Besselink, R., Stawski, T. M., Van Driessche, A. E. S. & Benning, L. G. Not just fractal surfaces, but surface fractal aggregates: Derivation of the expression for the structure factor and its applications. *The Journal of Chemical Physics* **145**, doi:10.1063/1.4960953 (2016).
- 42 Liu, Y., Paskevicius, M., Sofianos, M. V., Parkinson, G. & Li, C.-Z. In situ SAXS studies of the pore development in biochar during gasification. *Carbon* **172**, 454-462, doi:<https://doi.org/10.1016/j.carbon.2020.10.028> (2021).
- 43 Myers, A. L. & Prausnitz, J. M. Thermodynamics of mixed-gas adsorption. *AIChE Journal* **11**, 121-127, doi:<https://doi.org/10.1002/aic.690110125> (1965).
- 44 Krishna, R. Screening metal-organic frameworks for mixture separations in fixed-bed adsorbers using a combined selectivity/capacity metric. *RSC Advances* **7**, 35724-35737, doi:10.1039/C7RA07363A (2017).
- 45 Krishna, R. Metrics for Evaluation and Screening of Metal-Organic Frameworks for Applications in Mixture Separations. *ACS Omega* **5**, 16987-17004, doi:10.1021/acsomega.0c02218 (2020).
- 46 Kresse, G. & Furthmüller, J. Efficient iterative schemes for ab initio total-energy calculations using a plane-wave basis set. *Physical Review B* **54**, 11169-11186, doi:10.1103/PhysRevB.54.11169 (1996).
- 47 Kresse, G. & Joubert, D. From ultrasoft pseudopotentials to the projector augmented-wave method. *Physical Review B* **59**, 1758-1775, doi:10.1103/PhysRevB.59.1758 (1999).
- 48 Thonhauser, T. *et al.* Spin Signature of Nonlocal Correlation Binding in Metal-Organic Frameworks. *Physical Review Letters* **115**, 136402, doi:10.1103/PhysRevLett.115.136402 (2015).

Acknowledgements

This work was supported by the Robert A. Welch Foundation through an Endowed Chair to H.-C.Zhou (grant no. A-0030). H.W. acknowledges the funding from the National Natural Science Foundation of China (grant no. 22478251). Use of the Texas A&M University Soft Matter Facility (RRID: SCR_022482) and contributions of Dr. Peiran Wei and Dr. Jung Ahn are acknowledged. The authors acknowledge the characterization part of this work performed in the Texas A&M University Materials Characterization Core Facility (RRID: SCR_022202).

Author Contribution

The project was conceived and supervised by K.F., Q.W., and H.-C.Z. K.F. performed the main experiments and characterization of the sorbent. K.F., F.G., and H.W. conducted and analyzed the breakthrough measurement. K.F., H.L., and V.B. did the ss-NMR studies. S.U. and T.T. did the computational studies and K.F., S.U., and T.T. discussed the results. K.F., S.M. (Sayan Maiti), R.R., L.F., S.M. (Shengqian Ma) collected and analyzed the gas adsorption data. K.F., S.U., A.M., A.S., U.P., T.T., Q.W., and H.-C.Z. wrote the manuscript.

Competing Interests

The authors declare no competing interests.

Figure Legends/Captions (for main text figures)

Fig. 1. (a) Structure of PPN-20. The blue benzene (or rings) is from the monomer (1,3,5-Triacetylbenzene), while the light red rings are formed by the Aldol Triple Condensation reaction of the monomers' acetyl groups. (b) SAXS curve of PPN-20 fitted with Guinier approximation. (c) SAXS curve of PPN-20 fitted with the Porod approximation. The middle region in (b) represents the Guinier approximation with a radius of gyration ($14 \text{ \AA} = 1.4 \text{ nm}$), which shows that PPN-20 is microporous. The power-law exponent (c) obtained from the Porod equation is 2.13, which demonstrates that PPN-20 has a fractal surface. Source data are provided as a Source Data file.

Fig. 2. Minimal theoretical model of PPN-20. Top (a) and side views (b) of PPN-20 with the structural parameters calculated at the vdW-DF level. The blue region (3.782 \AA or 0.3782 nm) in the framework shows the pore size and structure of PPN-20, considering the influence of the C-H bond length on the pore. While this kind of pore size exists, bigger pores, as confirmed by the pore size distribution from N_2 adsorption at 77 K, are due to defects, random polymerization and monolayer stacking, and interpenetration of the bonds. As seen in the figure, **a** (red), **b** (green), and **c** (blue) vectors indicate the axes from which the monolayer can be viewed.

Fig. 3. Surface area, pore size distribution, and gas adsorption. (a) PPN-20 nitrogen isotherm at 77 K and 1 bar. (b) Pore size distribution derived from the nitrogen isotherm at 77 K and 1 bar. (c) Gas uptake of short-chain hydrocarbons. (d) Isothermic heat of adsorption of the short-chain hydrocarbons at 273 K, 298 K, and 1 bar. Source data are provided as a Source Data file.

Fig. 4. Breakthrough measurements. (a) The breakthrough curve of $\text{C}_2\text{H}_6/\text{C}_2\text{H}_4$ mixtures at 298 K and 1 bar. (b) The breakthrough curve of $\text{C}_3\text{H}_8/\text{C}_2\text{H}_6/\text{CH}_4$ mixtures at 298 K and 1 bar. (c) The multiple breakthrough cycling of $\text{C}_2\text{H}_6/\text{C}_2\text{H}_4$ at 298 K and 1 bar in PPN-20. (d) The multiple breakthrough cycle of $\text{C}_3\text{H}_8/\text{C}_2\text{H}_6/\text{CH}_4$ at 298 K and 1 bar in PPN-20.

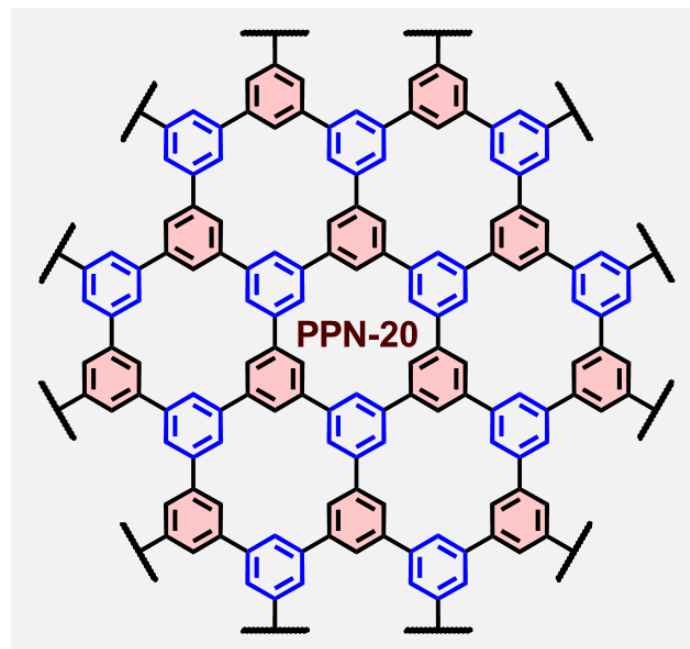
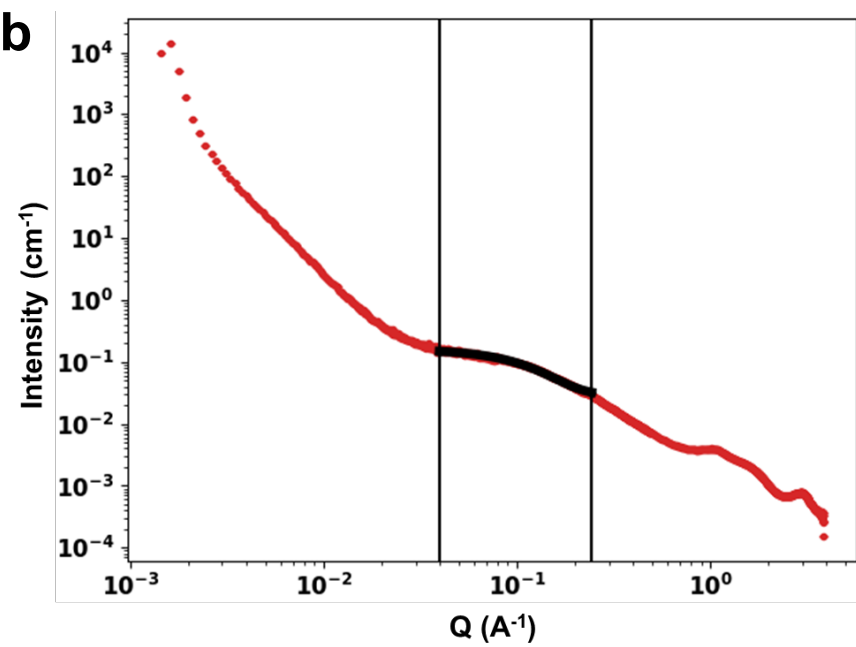
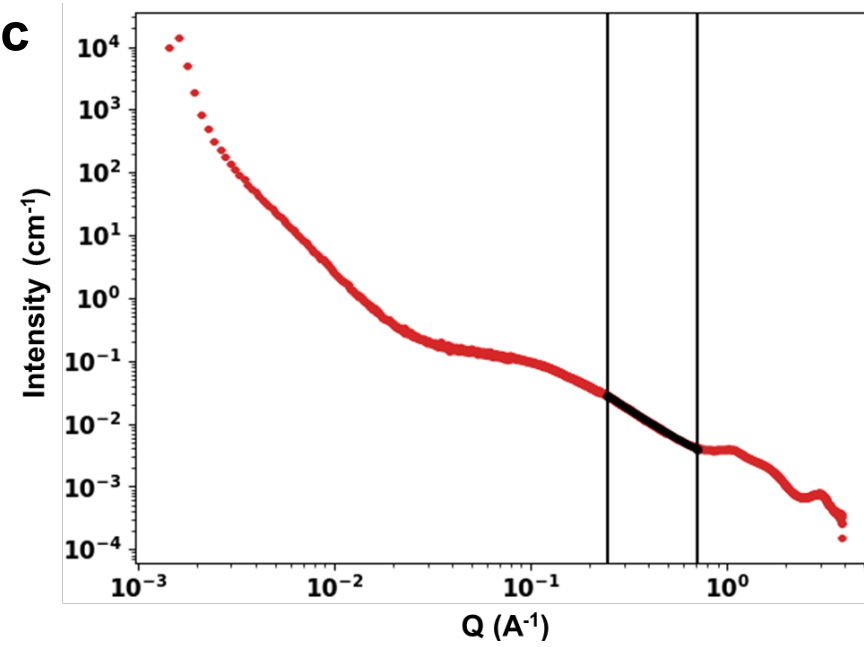
Fig 5. Preferred sites for gas adsorption. Optimized gas adsorption configurations on monolayer PPN-20. DFT-optimized structures showing (a) primary and (b) secondary preferred binding sites of the light hydrocarbons in PPN-20. Black (red) numbers in the "side view" indicate the closest distance from the carbon (hydrogen) atom of the adsorbed molecule to the sheet.

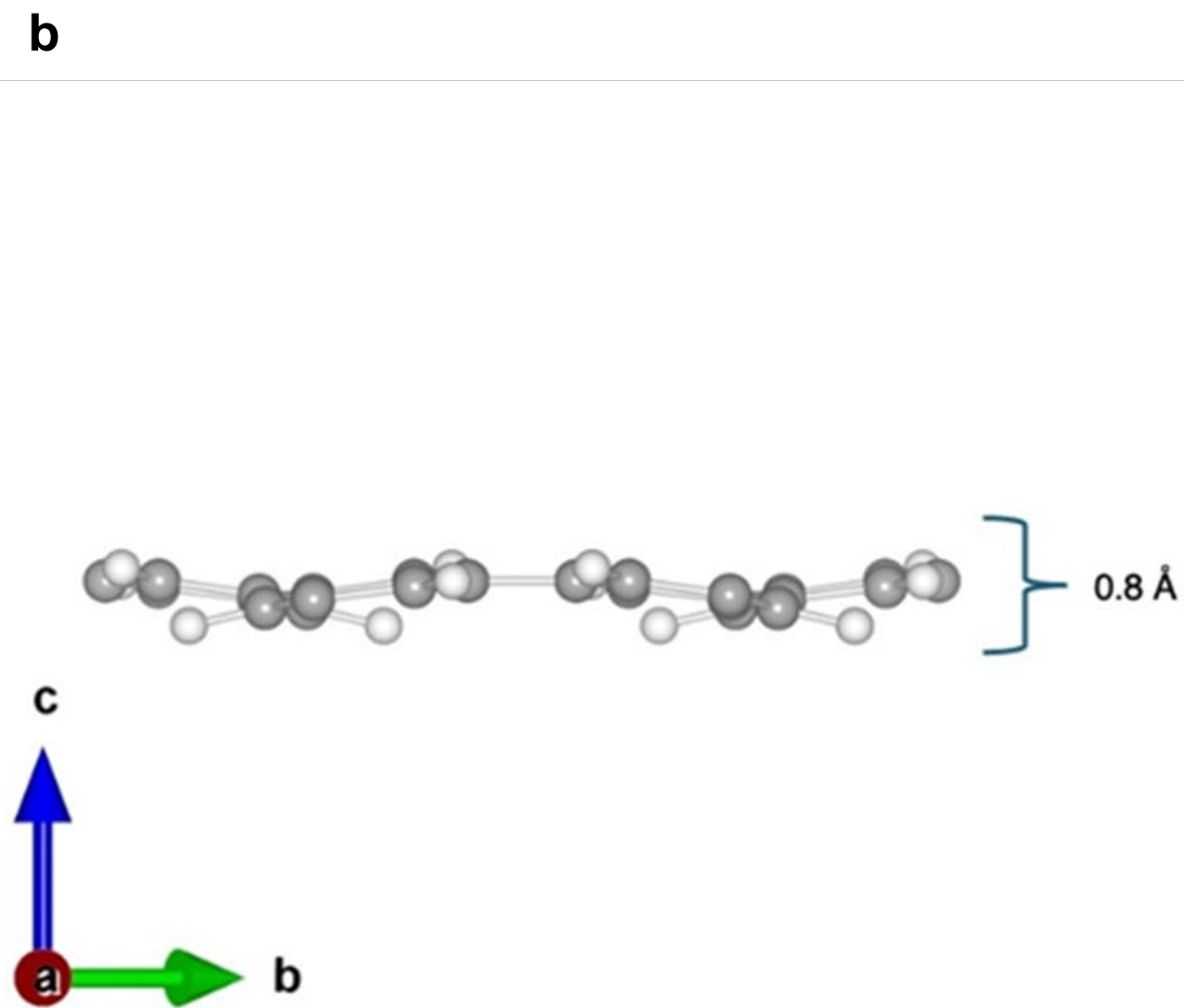
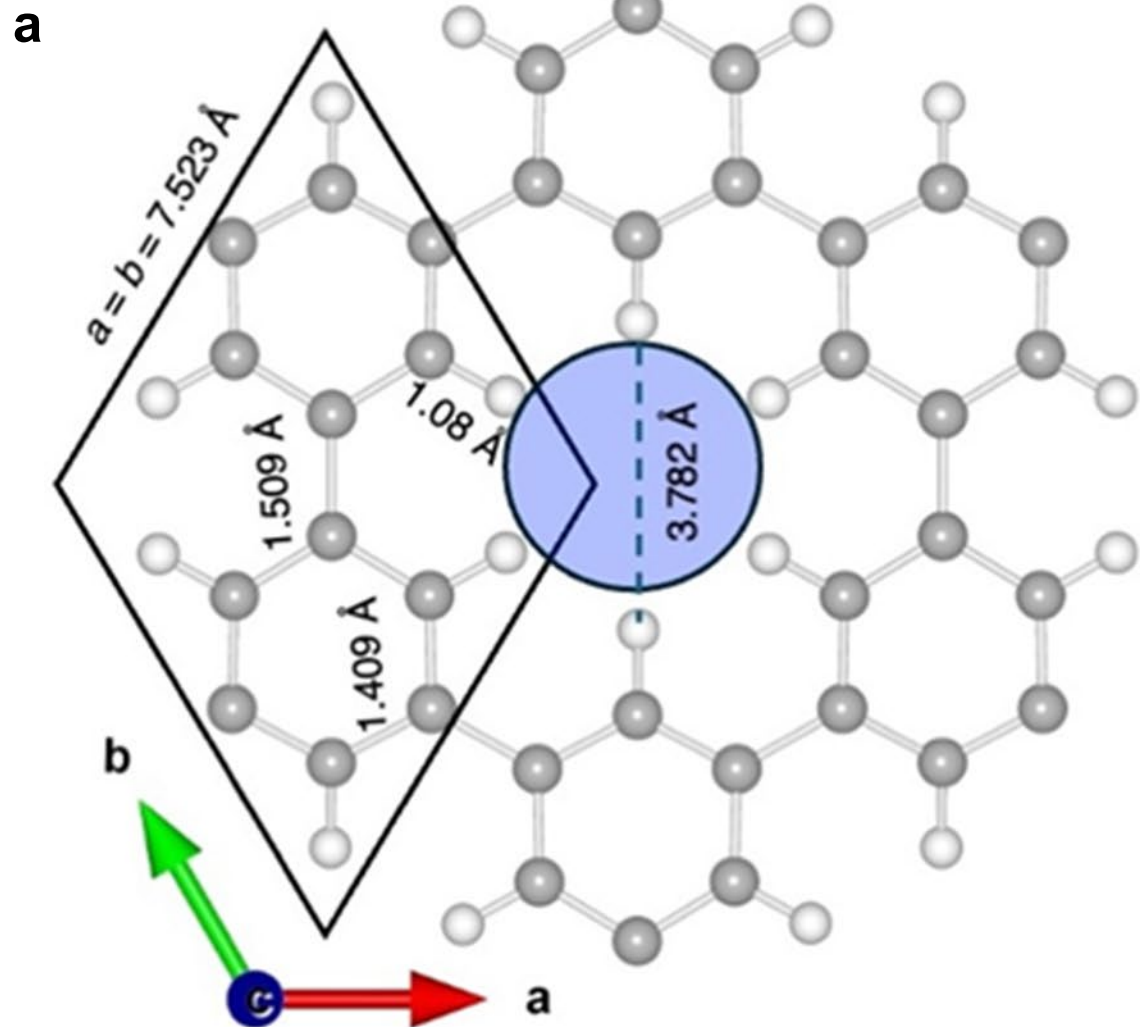
Editorial Summary

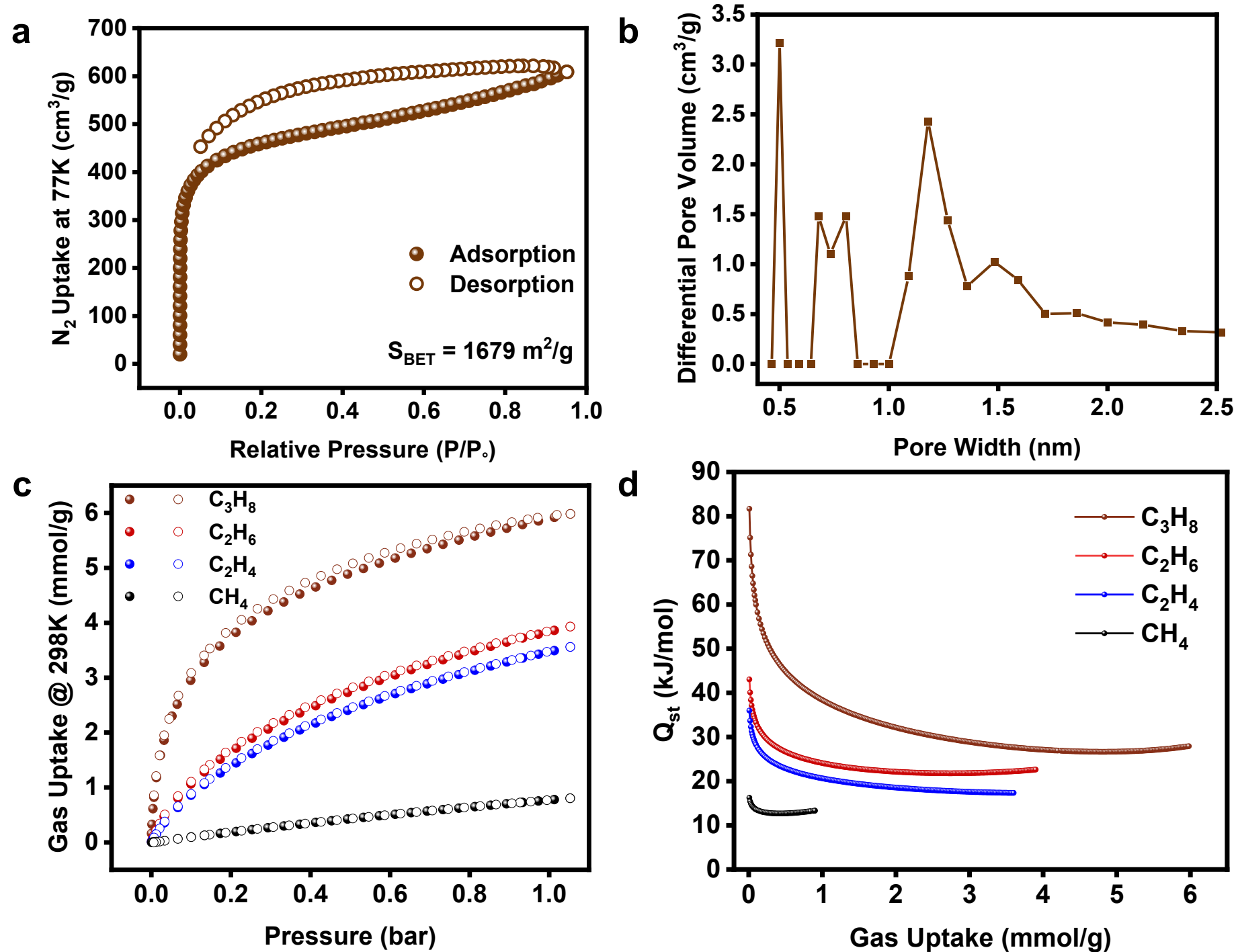
A graphene-inspired porous polymer network acts as a molecular sieve, efficiently separating ethane from ethylene and purifying methane. Its finely tuned pores deliver record selectivity, offering a new path toward cleaner natural gas processing.

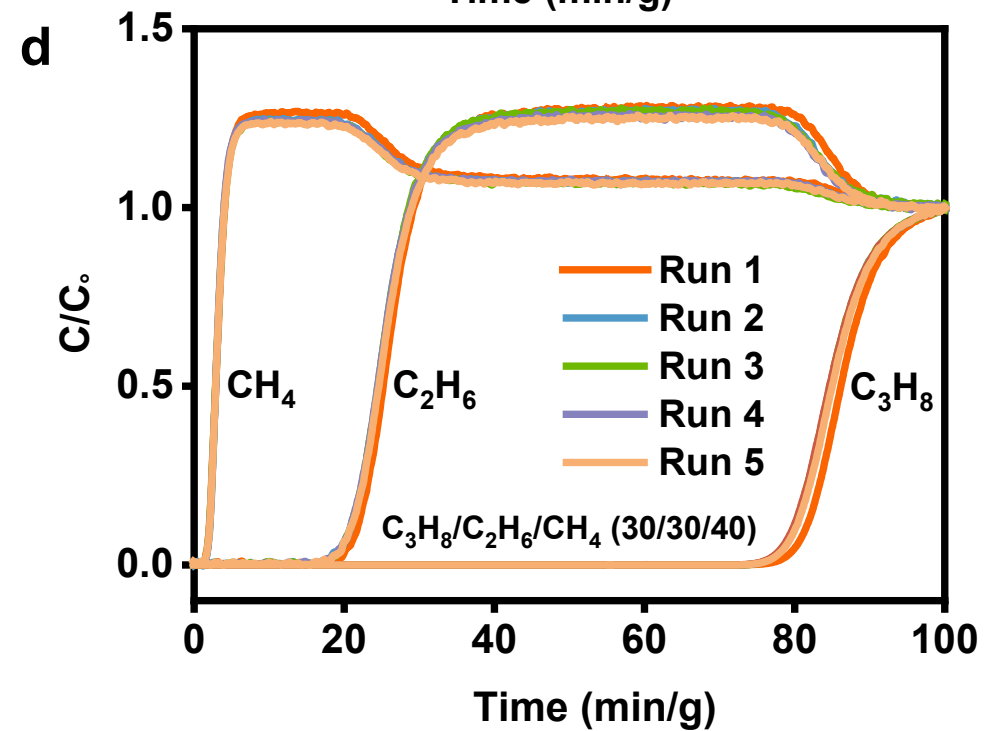
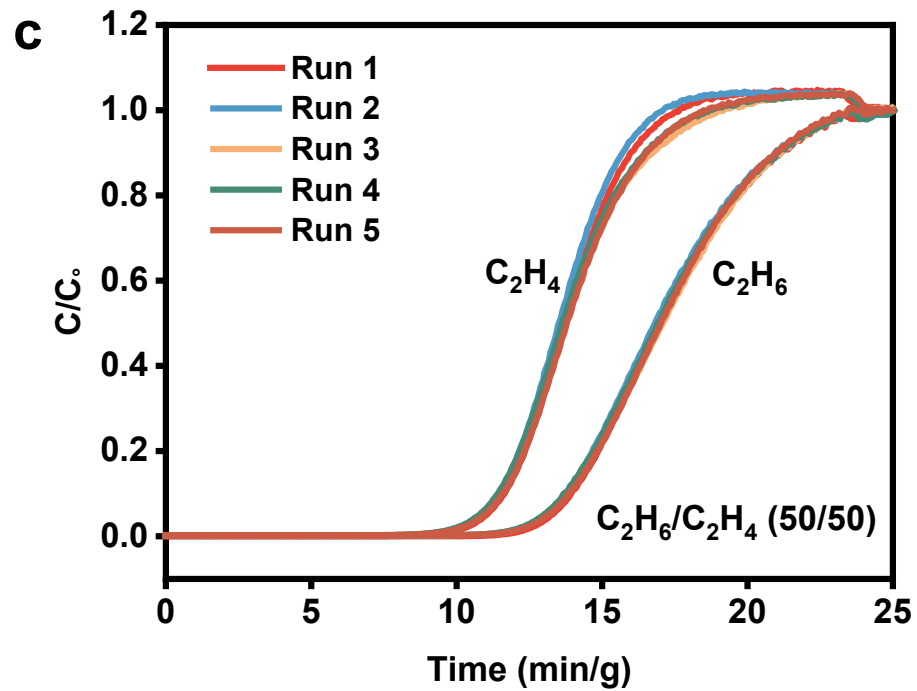
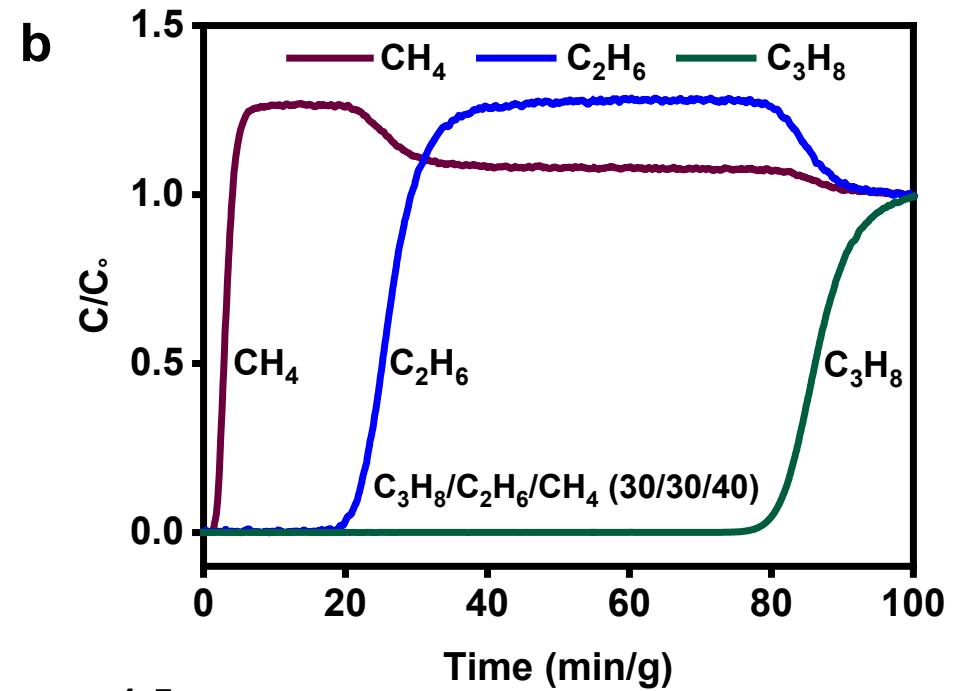
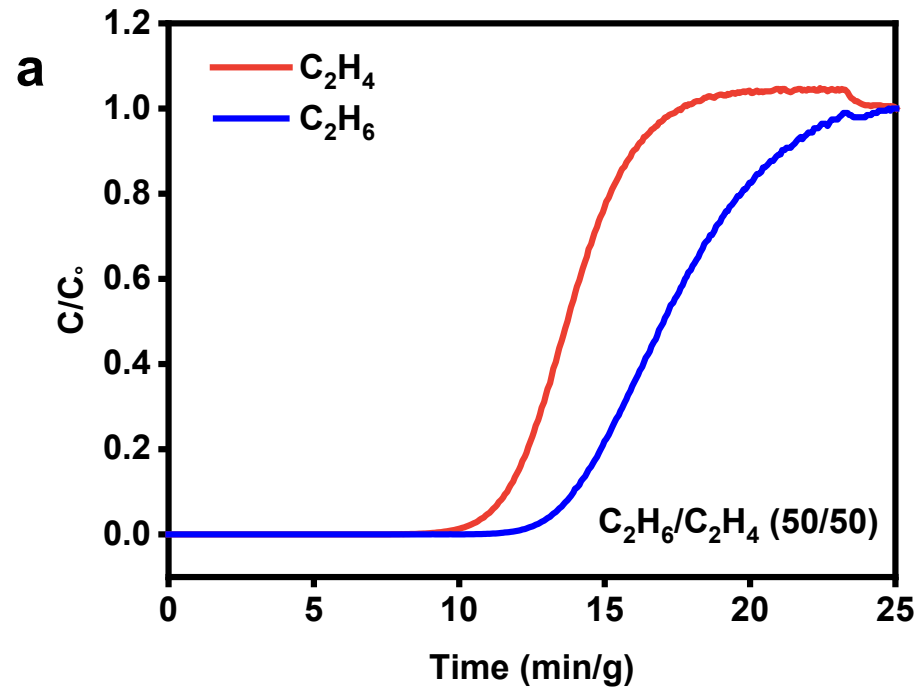
Peer Review Information: *Nature Communications* thanks Qibin Xia and the other, anonymous, reviewer(s) for their contribution to the peer review of this work. A peer review file is available.

ARTICLE IN PRESS

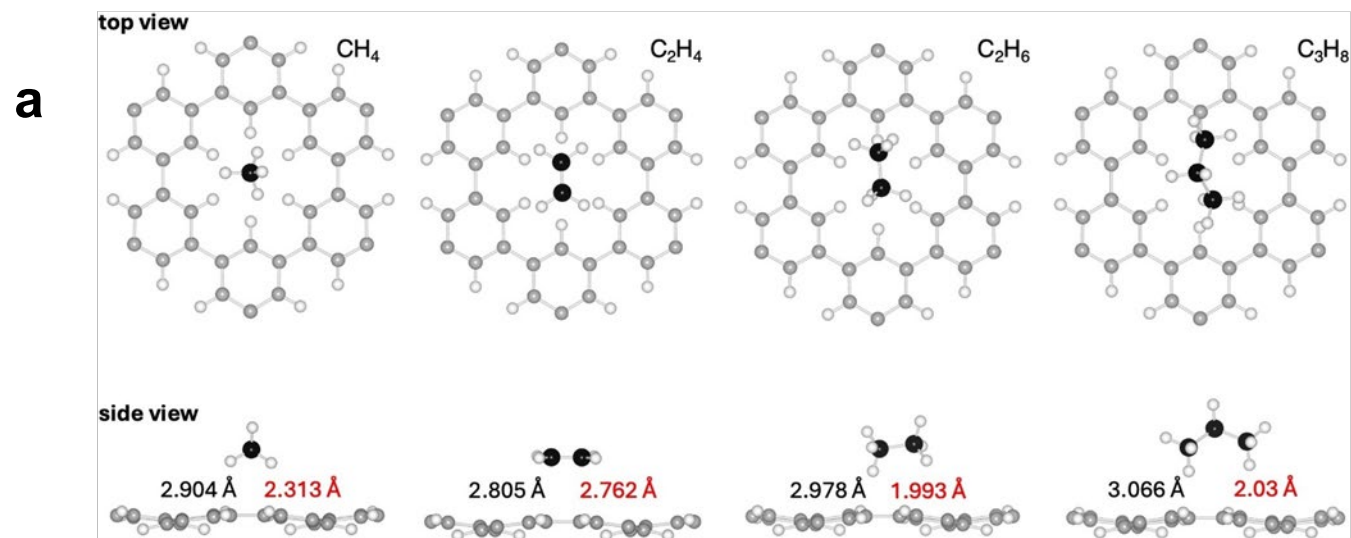
a**b****c**







Primary Binding Sites



Secondary Binding Sites

